Acta Crystallographica Section D
Biological Crystallography
ISSN 0907-4449

Structural and functional characterization of the N-terminal domain of the yeast Mg^{2+} channel Mrs2

Muhammad Bashir Khan,[a]‡ Gerhard Sponder,[b]§ Björn Sjöblom,[a] Soňa Svidová,[b] Rudolf J. Schweyen,[b]¶ Oliviero Carugo[a,c] and Kristina Djinović-Carugo[a,d]*

[a]Department of Structural and Computational Biology, Max F. Perutz Laboratories, University of Vienna, Vienna, Austria, [b]Department of Microbiology, Immunobiology and Genetics, Max F. Perutz Laboratories, University of Vienna, Vienna, Austria, [c]Department of Chemistry, University of Pavia, Pavia, Italy, and [d]Department of Biochemistry, Faculty of Chemistry and Chemical Technology, University of Ljubljana, Ljubljana, Slovenia

‡ Present address: Department of Biochemistry, University of Alberta, Edmonton, Alberta, Canada.
§ Present address: Institute of Veterinary Physiology, Freie Universität Berlin, Berlin, Germany.
¶ Deceased in February 2009.

Correspondence e-mail: kristina.djinovic@univie.ac.at

Received 9 March 2013
Accepted 29 April 2013

PDB Reference: $Mrs2_{48–308}$, 3rkg

Mg^{2+} translocation across cellular membranes is crucial for a myriad of physiological processes. Eukaryotic Mrs2 transporters are distantly related to the major bacterial Mg^{2+} transporter CorA, the structure of which displays a bundle of giant α-helices forming a long pore that extends beyond the membrane before widening into a funnel-shaped cytosolic domain. Here, a functional and structural analysis of the regulatory domain of the eukaryotic Mg^{2+} channel Mrs2 from the yeast inner mitochondrial membrane is presented using crystallography, genetics, biochemistry and fluorescence spectroscopy. Surprisingly, the fold of the Mrs2 regulatory domain bears notable differences compared with the related bacterial channel CorA. Nevertheless, structural analysis showed that analogous residues form functionally critical sites, notably the hydrophobic gate and the Mg^{2+}-sensing site. Validation of candidate residues was performed by functional studies of mutants in isolated yeast mitochondria. Measurements of the Mg^{2+} influx into mitochondria confirmed the involvement of Met309 as the major gating residue in Mrs2, corresponding to Met291 in CorA.

1. Introduction

Although the magnesium ion, Mg^{2+}, is essential to life, it remains the only major inorganic cation whose mechanism of transport is still not fully understood. It is present at high concentrations (15–25 m*M*) in prokaryotic and mammalian cells and is required for numerous cellular processes involved in cell architecture, cell growth, energy metabolism and replication (Cowan, 1991, 1998; Cowan *et al.*, 2000; Dann *et al.*, 2007; Quigley *et al.*, 1978). Maintenance of Mg^{2+} homeostasis is therefore critical for cell viability. Since cellular membranes are impermeable to Mg^{2+}, the involvement of various Mg^{2+}-transport mechanisms is required to mediate Mg^{2+} influx or efflux *via* plasmalemma and biomembranes forming subcellular compartments.

Members of the large heterogeneous CorA/Mrs2/Alr1 protein superfamily are found in prokaryotes and in both lower and higher eukaryotes, including plants. The CorA family of proteins mediates Mg^{2+} uptake in most prokaryotes and is the most extensively studied set of Mg^{2+} channels. The Mrs2 family of channels constitutes the major mitochondrial Mg^{2+}-uptake system in yeast, plants and mammals (Zsurka *et al.*, 2001; Kolisek *et al.*, 2003; Li *et al.*, 2001; Schock *et al.*, 2000) and is essential for mitochondrial biogenesis (Walker *et al.*, 1982). A third family of proteins, Alr1, is restricted to lower eukaryotes, where it forms the principal Mg^{2+}-uptake system in the plasma membrane. Although the overall sequence similarity of members of the CorA/Mrs2/Alr1 superfamily

is weak, these proteins appear to exploit the membrane potential in driving Mg^{2+} uptake (Kolisek *et al.*, 2003; Froschauer *et al.*, 2004) and can in part functionally replace each other, which strongly suggests that they are functionally and structurally conserved (Bui *et al.*, 1999; Zsurka *et al.*, 2001; Kehres & Maguire, 2002; Li *et al.*, 2001; Eshaghi *et al.*, 2006).

The crystal structures of *Thermotoga maritima* CorA (Tm-CorA; Lunin *et al.*, 2006; Eshaghi *et al.*, 2006; Payandeh & Pai, 2006) and of *Methanocaldococcus jannaschii* CorA (Mj-CorA; Pfoh *et al.*, 2012; Guskov *et al.*, 2012) and the structures of the soluble cytoplasmic domains of the zinc transporters of *Vibrio parahemolyticus* (Vp-ZntB; Tan *et al.*, 2009) and *Salmonella enterica* serovar Typhimurium (St-ZntB; Wan *et al.*, 2011) have revealed homopentamers. The crystal structure of Tm-CorA diplays a funnel-shaped assembly with the stem of the funnel in the membrane. The N-terminal cytoplasmic domain, consisting of about 250 amino acids, is followed by two transmembrane segments (TM1 and TM2) connected by a nine-amino-acid periplasmic loop and a short six-amino-acid cytosolic C-terminus. The pore is essentially formed by five parallel helices of TM1, while the five N-terminal domains form the funnel. Conversely, the structures of the cytoplasmic domains of Tm-CorA (Lunin *et al.*, 2006), of *Archaeoglobus fulgidus* CorA (Af-CorA; Payandeh & Pai, 2006) and of St-ZntB crystallized at higher ionic strengths (Wan *et al.*, 2011) show a dimeric arrangement of the subunits, which might be an effect of the crystallization conditions.

Ion selectivity remains unclear despite numerous studies. The conserved GMN sequence motif at the end of the TM1 α-helix on the outer surface of the membrane is considered to be essential for Mg^{2+} recognition (Kehres *et al.*, 1998; Worlock & Smith, 2002), perhaps in cooperation with the following negatively charged residues (Lunin *et al.*, 2006; Eshaghi *et al.*, 2006; Payandeh & Pai, 2006; Zhang & Mu, 2012). The presence of an Mg^{2+} cation solvated by a first coordination sphere of water molecules has been observed close to the asparagine and glycine in some of the crystal structures of CorA, supporting the hypothesis that the GMN motif plays a direct role in recognizing Mg^{2+} cations and perhaps in preventing other species from entering the pore (Pfoh *et al.*, 2012; Guskov *et al.*, 2012). However, a sound explanation of cation selectivity is still lacking.

A pair of hydrophobic rings that are formed by Met291 and Leu294 in the pentamer have been suggested to be involved in the gating of the channel (Lunin *et al.*, 2006; Eshaghi *et al.*, 2006; Payandeh & Pai, 2006; Guskov *et al.*, 2012) and it has been proposed that the opening and closing of the channel is regulated by the overall architecture of the pentameric protein rather than by a small number of residues (Chakrabarti *et al.*, 2010).

On the basis of numerous studies, there is a general agreement that regulation of CorA depends on the intracellular Mg^{2+} concentration (Eshaghi *et al.*, 2006; Payandeh & Pai, 2006; Lunin *et al.*, 2006; Payandeh *et al.*, 2008; Palombo *et al.*, 2012). Mg^{2+} cations are believed to bridge adjacent N-terminal domains of Tm-CorA, which become more flexible and free to relax from each other on a decrease in the Mg^{2+} concentration (Chakrabarti *et al.*, 2010). Their structural rearrangement would be responsible for the pore opening. However, the detailed mechanism of the relationship between the N-terminal domain rearrangements and the pore gating is still under debate (Eshaghi *et al.*, 2006; Payandeh & Pai, 2006, Lunin *et al.*, 2006; Payandeh *et al.*, 2008; Palombo *et al.*, 2012). Complex structural plasticity of the intracellular ring formed by the five N-terminal rigid bodies was recently observed experimentally in the crystal structure of a Tm-CorA mutant determined in the absence of Mg^{2+}. The concerted movements in the N-terminal domain at low intracellular Mg^{2+} concentrations were proposed to eventually lead to bending of the long pore-forming helix 7 and to opening of the channel (Pfoh *et al.*, 2012). Less complex movements were suggested based on the structure of Mj-CorA. According to this model opening of the channel is mediated by a turn of TM1, resulting in the replacement of hydrophobic residues facing the inside of the pore with polar residues and resulting in a hydrophilic environment allowing the influx of Mg^{2+} (Guskov *et al.*, 2012).

The sequence homology between the eukaryotic and the prokaryotic channels seems to be most pronounced in the transmembrane region and in the signature GMN motif, while the sequences in the N-terminal region are more divergent, which renders it difficult to infer structural/functional information on Mrs2 based on the prokaryotic template. For this reason, we determined the crystal structure of the regulatory N-terminal domain of the yeast (*Saccharomyces cerevisiae*) mitochondrial Mg^{2+} channel Mrs2 at 1.28 Å resolution. Furthermore, several mutants were designed and functionally characterized in the whole cell and in isolated yeast mitochondria in order to validate their hypothetical roles in gating and metal sensing.

2. Experimental procedures

2.1. Protein expression and purification

Details of the cloning and purification have been reported previously (Khan *et al.*, 2010). The mitochondrial matrix domain of *S. cerevisiae* was cloned from genomic DNA into pETM-11 vector (EMBL Hamburg) with a *Tobacco etch virus* (TEV) protease-cleavable N-terminal His_6 tag. The recombinant protein was overexpressed in *E. coli* BL21 Star (DE3) cells at 294 K in the presence of 0.025 mg ml^{-1} kanamycin and induced with 0.5 m*M* isopropyl β-D-1-thiogalactopyranoside (IPTG). Cells were sonicated in a suitable buffer. The supernatant after centrifugation was applied onto a 5 ml Ni–NTA agarose column (Qiagen). The N-terminal His_6 tag was cleaved using TEV protease. After TEV protease cleavage, the protein was reapplied onto an Ni–NTA column, followed by anion-exchange chromatography, in which the sample was loaded onto a Resource Q column (6 ml; GE Healthcare) equilibrated with washing buffer consisting of 50 m*M* Tris–HCl pH 8.0, 20 m*M* NaCl, 5 m*M* BME, 1 m*M* PMSF, 5% glycerol. The protein was eluted using a gradient of 20–1000 m*M* NaCl in 50 m*M* Tris–HCl pH 8.0, 5 m*M* BME, 1 m*M* PMSF, 5% glycerol. The sample was then applied onto a

Table 1
Data-collection and refinement statistics.

Values in parentheses are for the highest resolution shell.

	Data set 1	Data set 2
Data collection		
Source	Home source	ID14-1, ESRF
Wavelength (Å)	1.541	0.933
Resolution (Å)	36.9–1.83 (1.90–1.83)	50.0–1.28 (1.35–1.28)
Space group	$P2_12_12_1$	$P2_12_12_1$
Unit-cell parameters (Å)	a = 54.66, b = 61.70, c = 85.30	a = 54.88, b = 61.88, c = 85.45
Molecules per asymmetric unit	1	1
Unique reflections	48844	69621 (4235)
Completeness (%)	99.0 (92.0)	92.1 (79.0)
$R_{\rm meas}$†		0.069 (1.172)
$R_{\rm p.i.m.}$‡	0.80 (23.0)	
$R_{\rm anom}$	0.0316	
Multiplicity	80.0 (13.0)	12.0 (6.2)
$\langle I/\sigma(I)\rangle$	40.2 (1.9)	19.9 (1.83)
Phasing		
No. of sites	11	
Phasing power§	0.311 (0.069)	
Figure of merit	0.841	
Refinement		
$R_{\rm cryst}$¶/$R_{\rm free}$††	0.193/0.244	0.169/0.204
No. of reflections used for $R_{\rm free}$	1289	7312
R.m.s.d., bonds (Å)	0.0124	0.004
R.m.s.d., angles (°)	1.33	0.91
B, protein (Å^2)	29.6	15.1

† $R_{\rm meas} = \sum_{hkl}\{N(hkl)/[N(hkl)-1]\}^{1/2}\sum_i |I_i(hkl)-\langle I(hkl)\rangle|/\sum_{hkl}\sum_i I_i(hkl)$. ‡ $R_{\rm p.i.m.} = \sum_{hkl}\{1/[N(hkl)-1]\}^{1/2}\sum_i |I_i(hkl)-\langle I(hkl)\rangle|/\sum_{hkl}\sum_i I_i(hkl)$, where $\langle I(hkl)\rangle$ is the mean intensity of multiple observations $I_i(hkl)$ of symmetry-related reflections and $N(hkl)$ is the redundancy. § Anomalous phasing power = $[\sum |F_{\rm H}({\rm imag})|^2/\sum ||\Delta F\pm_{\rm PH}({\rm obs})| - |\Delta F\pm_{\rm PH}({\rm obs})||^2]^{1/2}$, where $\Delta F\pm_{\rm PH}$ is the structure-factor difference between Bijvoet pairs and $F_{\rm H}$(imag) is the imaginary component of the calculated structure-factor contribution from the anomalously scattering atoms. ¶ $R_{\rm cryst} = \sum_{hkl}||F_{\rm obs}|-|F_{\rm calc}||/\sum_{hkl}|F_{\rm obs}|$. †† $R_{\rm free}$ is the cross-validation R factor computed for a test set of reflections (5%) which were omitted in the refinement process.

HiLoad 26/60 Superdex 200 (GE Healthcare) size-exclusion chromatography column equilibrated with a buffer composed of 50 m*M* Tris–HCl pH 8.0, 300 m*M* NaCl, 5% glycerol. The purified protein was concentrated to 3 mg ml^{-1} for crystallization screening by reapplying it onto a Resource Q column (6 ml; GE Healthcare) as described above.

2.2. Protein purity and monodispersity controls

The purity of the protein solution used in the crystallization experiments was evaluated by SDS–PAGE analysis and showed a single band with an apparent molecular weight of about 30 kDa. Dynamic light scattering (DLS) was used to assess the monodispersity of the protein solution: a monomodal distribution with a polydispersity of 5% was observed and the radius of gyration was estimated to be 4.2 nm, suggesting that the protein solution was homogenous and monomeric in 50 m*M* Tris–HCl pH 8.0, 300 m*M* NaCl, 5% glycerol. At low salt concentrations (15 m*M* Tris–HCl pH 8.0, 15 m*M* NaCl, 5% glycerol) the protein solution exhibited a polydispersity of about 25% and a radius of gyration of 14 nm, suggestive of a pentameric form. Circular-dichroism (CD) spectroscopy in the far-ultraviolet wavelength range showed that the protein is rich in α-helical content.

2.3. Analytical gel-filtration chromatography

Analytical gel-filtration chromatography of Mrs2$_{48–308}$ was performed at 277 K using the construct eluted as a monomer from the Superdex 200 10/300 column (GE Healthcare) in a buffer consisting of 50 m*M* Tris–HCl pH 8.0, 300 m*M* NaCl, 5% glycerol, 1 m*M* PMSF. After dialyzing the protein against low ionic strength buffer (15 m*M* Tris–HCl pH 8.0, 5 m*M* NaCl, 5% glycerol, 1 m*M* PMSF) and running on the same analytical size-exclusion chromatography column (Superdex 200 10/300 column; GE Healthcare) in 15 m*M* Tris–HCl pH 8.0, 15 m*M* NaCl, 1 m*M* PMSF, 5% glycerol, the protein eluted as a pentamer. Prior to experiments, the column was calibrated with high-salt and low-salt buffer, respectively.

2.4. Crystallization

Details of the crystallization conditions have been reported previously (Khan *et al.*, 2010). Initial crystallization screening conditions obtained by sparse-matrix screening using the MembFac kit (Hampton Research) were optimized by the hanging-drop method at 295 K. Mg^{2+}-soaked and Co^{2+}-soaked crystals were obtained by soaking the native crystal with 1–5 m*M* magnesium chloride and 5 m*M* cobalt chloride in the crystallization drops. Cocrystals with Mg^{2+} or Co^{2+} ions were grown by vapour diffusion at 295 K in a solution consisting of 2.8 mg ml^{-1} protein, 22%(*v*/*v*) ethylene glycol, 56 m*M* sodium/potassium phosphate pH 6.3, 1.5 m*M* magnesium chloride or cobalt chloride. Crystals were flash-cooled in a solution consisting of 30%(*v*/*v*) ethylene glycol, 56 m*M* sodium/potassium phosphate pH 6.3 and mounted on loops at 100 K prior to data collection.

2.5. Data collection, structure solution and refinement

X-ray diffraction data sets for Mrs2$_{48–308}$ were collected at 100 K in a cold nitrogen stream using various beamlines at ESRF or a MICROSTAR rotating-anode generator at 1.54 Å wavelength. The crystals of Mrs2$_{48–308}$ diffracted to 1.83 Å resolution on the in-house source and to 1.28 Å resolution at ESRF. Details of the data collection, statistics and processing have been reported previously (Khan *et al.*, 2010). In brief, crystallographic data collected in-house were processed (integrated and scaled) with the *PROTEUM*2 software suite (Bruker AXS), while the synchrotron data sets were processed using *XDS* (Kabsch, 2010). The structure of Mrs2$_{48–308}$ was solved using a highly redundant data set collected on an in-house source by the single-wavelength anomalous dispersion method (SAD) exploiting the Mrs2 native S atoms for phasing using *SHELXD* (Usón & Sheldrick, 1999). After finding the S atoms, heavy-atom refinement and density modification were performed using *autoSHARP* (Vonrhein *et al.*, 2007). The electron-density map obtained from *autoSHARP* was traced by *ARP*/*wARP* (Morris *et al.*, 2003; Joosten *et al.*, 2008), which fitted 243 of 261 amino-acid residues in three different chains with $R_{\rm work}$ and $R_{\rm free}$ values of 0.21 and 0.30, respectively. The structure refinement yielded final $R_{\rm work}$ and $R_{\rm free}$ values of 0.193 and 0.243, respectively. This model contained 258 amino-acid residues and 432 water molecules. Two complete data sets

to 1.42 and 1.28 Å resolution were collected on beamline 14-1 at ESRF and were processed individually using *XDS*. The data sets were then scaled together using *SCALA*. The structure from the S-SAD data was further refined against the merged 1.28 Å resolution data sets using *REFMAC*5 and *PHENIX*. The final model contains 261 amino acids, 392 water molecules and five ethylene glycol molecules with a R_{work} and an R_{free} of 0.169 and 0.204, respectively. Details of the data-collection and refinement statistics are given in Table 1.

2.6. Construction of the Mrs2 pentamer

The three-dimensional model of the full-length Mrs2 pentamer was built in the following successive steps.

(i) The α-helix was extended at the C-terminus of the crystal structure of the $Mrs2_{48–308}$ domain, starting at Arg305 and ending at the GMN motif, with the program *SPDV* (Guex & Peitsch, 1997) (this is referred to as model *A*).

(ii) A three-dimensional model of the two transmembrane helices of Mrs2 was built with the program *Modeller* using the structure of Tm-CorA (PDB entry 2iub; Eshaghi *et al.*, 2006) as a template (chain *A*) and the sequence alignment shown in Fig. 2(*c*) (this is referred to as model *B*). The loop intercalated in between the two transmembrane helices was not modelled, since it is absent from the template and is likely to be conformationally very flexible or even disordered.

(iii) The first transmembrane helix of model *B* was superposed on the first transmembrane helix of model *A* in order to merge these two models and produce an entire protomer of Mrs2 (this is referred to as model *C*).

(iv) The pentameric Mrs2 was built by superimposing the transmembrane helices of model *C* with the transmembrane helices of the Tm-CorA pentamer.

2.7. Protease-susceptibility assay

For 50 µl reaction volumes, stock solutions were prepared to obtain the final concentration desired upon dilution: 39 µl protein solution (2.5 mg ml^{-1}), 1 µl trypsin solution (10 mg ml^{-1}; Sigma) and 10 µl of 0–100 m*M* metal solution. Reaction solutions were mixed and equilibrated at 277 K for 20 min. Trypsin was then added and the reactions were incubated at 277 or 310 K for the desired times. After adding 50 µl SDS–PAGE sample buffer, samples were boiled and run immediately on 15% SDS–PAGE gels. In order to rule out the possibility of trypsin inhibition, controls were performed on the test protein bovine serum albumin (BSA) over the full range of conditions.

2.8. Yeast strains, growth media and genetic procedures

S. cerevisiae strain DBY747 and the isogenic deletion strain *mrs2*Δ have been described previously (Bui *et al.*, 1999; Wiesenberger *et al.*, 1992). Yeast cells were grown in YPD medium (1% yeast extract, 2% peptone, 2% glucose) to stationary phase. For growth tests on solid medium, yeast cells were grown in YPD medium overnight, washed with dH_2O, spotted in tenfold dilutions on YPD medium or YPG medium (1% yeast extract, 2% peptone, 3% glycerol) and incubated at 301 K for 3 d (YPD) or 6 d (YPG).

2.9. Plasmid constructs

The plasmid YEp351-*MRS2*-HA (Bui *et al.*, 1999) was used as the template in overlap extension PCR. Mutagenic forward and reverse primers are reported in the Supplementary Material[1]. Verification of positive clones was performed by restriction analysis of the introduced *Eco*RI (Met309 and Val315) or *Ava*I (Asp97) sites (underlined). All restriction sites were introduced by silent mutations. No additional mutations were found by sequencing of the complete ORF. PCR fragments were digested with *Xba*I and *Sma*I and cloned into the vectors YEp351-*MRS2*-HA and YCp22-*MRS2*-HA digested with the same enzyme combination.

2.10. Isolation of mitochondria and measurement of $[Mg^{2+}]_m$ by spectrofluorimetry

Isolation of mitochondria and the ratiometric determination of intramitochondrial Mg^{2+} concentrations ($[Mg^{2+}]_m$) dependent on various external concentrations ($[Mg^{2+}]_e$) were performed as reported previously (Kolisek *et al.*, 2003).

2.11. Miscellaneous

The SBSA (structure-based sequence alignment) was made with *SHEBA* (*Structural Homology by Environment-Based Alignment*; Jung & Lee, 2000). $Mrs2_{48–308}$ and Tm-CorA were first aligned by *SHEBA*. The two aligned sequences were then aligned with randomly selected sequences of ten eukaryotic and ten prokaryotic Mg^{2+} channels using the profile-alignment features of *ClustalX*2 (Larkin *et al.*, 2007). The resulting alignments were manually reviewed. Sequence identity and conservation were determined using the *LALIGN* web server (Pearson, 1991) and *ESPript* (Gouet *et al.*, 2003), respectively.

3. Results and discussion

3.1. Ionic strength modulates the oligomeric state of $Mrs2_{48–308}$

Based on our study (Khan *et al.*, 2010), we designed a stable Mrs2 construct containing the polypeptide segment from residue 48 to residue 308 (referred to as $Mrs2_{48–308}$; see Fig. 1*a*). This construct was termed $Mrs2_{16–276}$ in our previous publication (in which the mitochondrial targeting sequence was not included in the numbering) and includes the entire regulatory N-terminal domain of Mrs2.

The circular-dichroism (CD) spectrum of $Mrs2_{48–308}$ showed minima at 208 and 219 nm typical for a protein rich in α-helices (Supplementary Fig. S1). On analytical size-exclusion chromatography $Mrs2_{48–308}$ behaves as a monomer at high salt concentration (300 m*M* NaCl) and as a pentamer at low salt concentration (15 m*M* NaCl) (Supplementary

[1] Supplementary material has been deposited in the IUCr electronic archive (Reference: DZ5283). Services for accessing this material are described at the back of the journal.

Fig. S2). Dynamic light scattering (DLS) was used to assess the monodispersity of the protein in solution: a monomodal distribution with a polydispersity of 5% was observed at high salt concentration, where the gyration radius was estimated to be 4.2 nm. At low salt concentration the protein solution exhibited a polydispersity of about 25% and a radius of gyration of 14 nm, which is consistent with the analytical size-exclusion chromatography profile (Supplementary Fig. S2). These data suggest that our construct is autonomously folded into the native conformation in solution and that the protein solution is monomeric at high ionic strength and pentameric at low ionic strength. The same was observed for *S. enterica* serovar Typhimurium zinc channel (StZntB), in which the pentameric state is disrupted at high salt concentrations (Wan *et al.*, 2011), suggesting that polar interactions are important for the stability of the oligomeric state of Mrs2.

3.2. Structure of $Mrs2_{48–308}$

The N-terminal domain $Mrs2_{48–308}$ crystallized in the orthorhombic space group $P2_12_12_1$. Its structure was solved by experimental phasing exploiting the sulfur anomalous signal using an in-house X-ray source (Khan *et al.*, 2010) and was refined to 1.28 Å resolution with diffraction data collected using synchrotron radiation (Table 1, Fig. 1*b*). The unit cell contains one molecule per asymmetric unit. Residues 48–305 are visible in the electron-density maps.

3.3. Comparison with CorA: the N-terminal domain of Mrs2 adopts a distinct fold

The overall organization of prokaryotic (Tm-CorA) and eukaryotic ($Mrs2_{48–308}$) Mg^{2+} channels is similar. Each subunit can be divided into an N-terminal α/β domain that is followed by an α-helical domain. While the former is a compact α-β-α sandwich, the latter forms a triple coiled coil, the end of which enters the membrane with a TM1 helix (Figs. 1*b*–1*e*).

While the coiled-coil domains in Tm-CorA and $Mrs2_{48–308}$ are nearly identical, the N-terminal domains differ notably (Figs. 1*c* and 1*e*). The central β-sheet is formed by seven strands in Tm-CorA *versus* six strands in $Mrs2_{48–308}$. Whereas the last four β-strands (termed C1–C4 in Figs. 1*c* and 1*e*) are topologically identical in both proteins and form a series of three β-hairpins, the first two β-strands differ topologically. The α-helix that follows the N2 strand and the entire N3 strand are missing in $Mrs2_{48–308}$, rendering the eukaryotic protein smaller than its prokaryotic counterpart. Although this disparity appears to have arisen owing to a deletion during molecular evolution, we cannot exclude other hypotheses. However, from this analysis it is clear that any automatic structural sequence alignments of these domains will be misleading because Tm-CorA and Mrs2 adopt different folds.

The relatively long α5 and α6 helices, which extend toward the membrane, are called 'willow' helices in Tm-CorA as they 'hang down like the branches of a weeping willow tree' and harbour many glutamic and aspartic acid

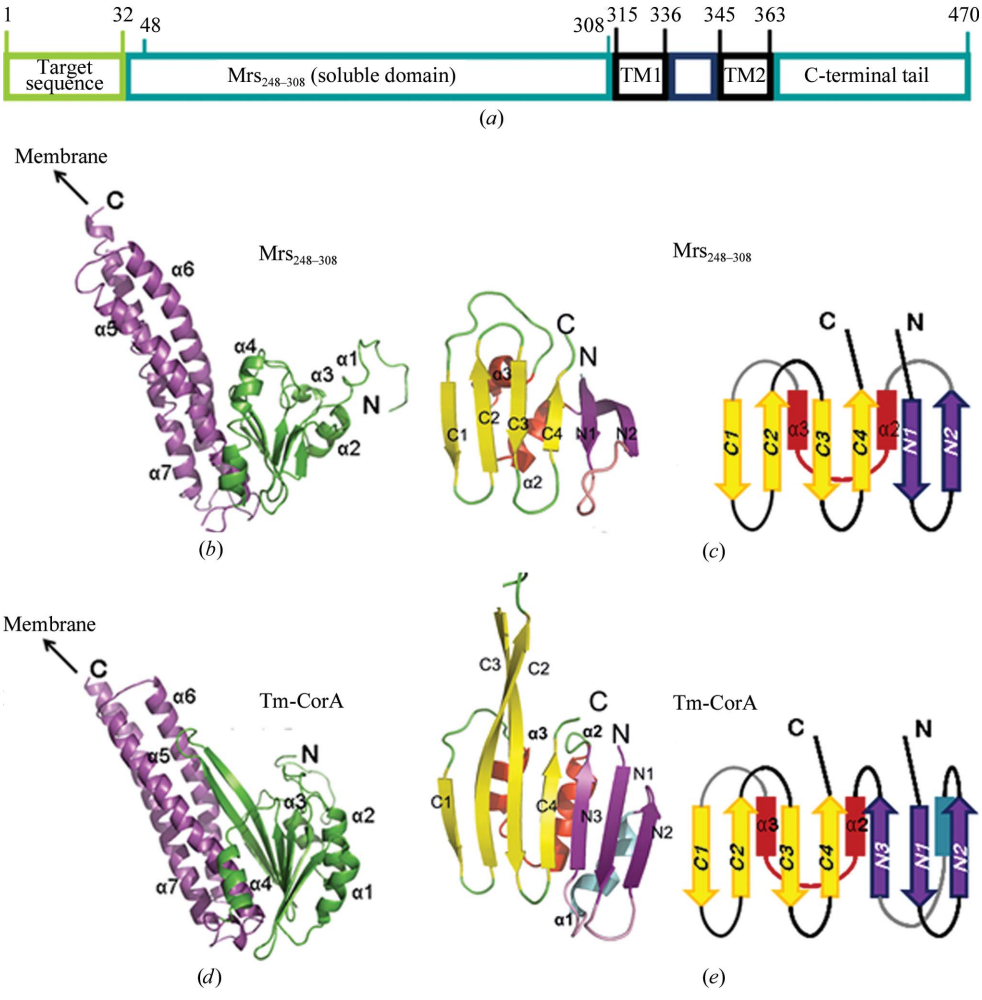

Figure 1
Structure of the N-terminal domain of Mrs2 and structural comparison with its closest structural homologue Tm-CorA. (*a*) A schematic view of the domain structure of Mrs2. (*b*) Structure of the N-terminal domain of Mrs2 comprising residues 48–308. The C-terminal triple coiled coil which continues into the membrane is coloured magenta and the N-terminal $\alpha/\beta/\alpha$ domain is coloured green. (*c*, *d*, *e*) Comparison of the N-terminal domains of Tm-CorA and $Mrs2_{48–308}$. While the last four β-strands (C1–C4; yellow) are topologically identical, there are two β-strands in Mrs2 (N1 and N2; magenta) and three in Tm-CorA (N1–N3; magenta). The α-helix which is intercalated between the second and the third strands of Tm-CorA is missing in $Mrs2_{48–308}$.

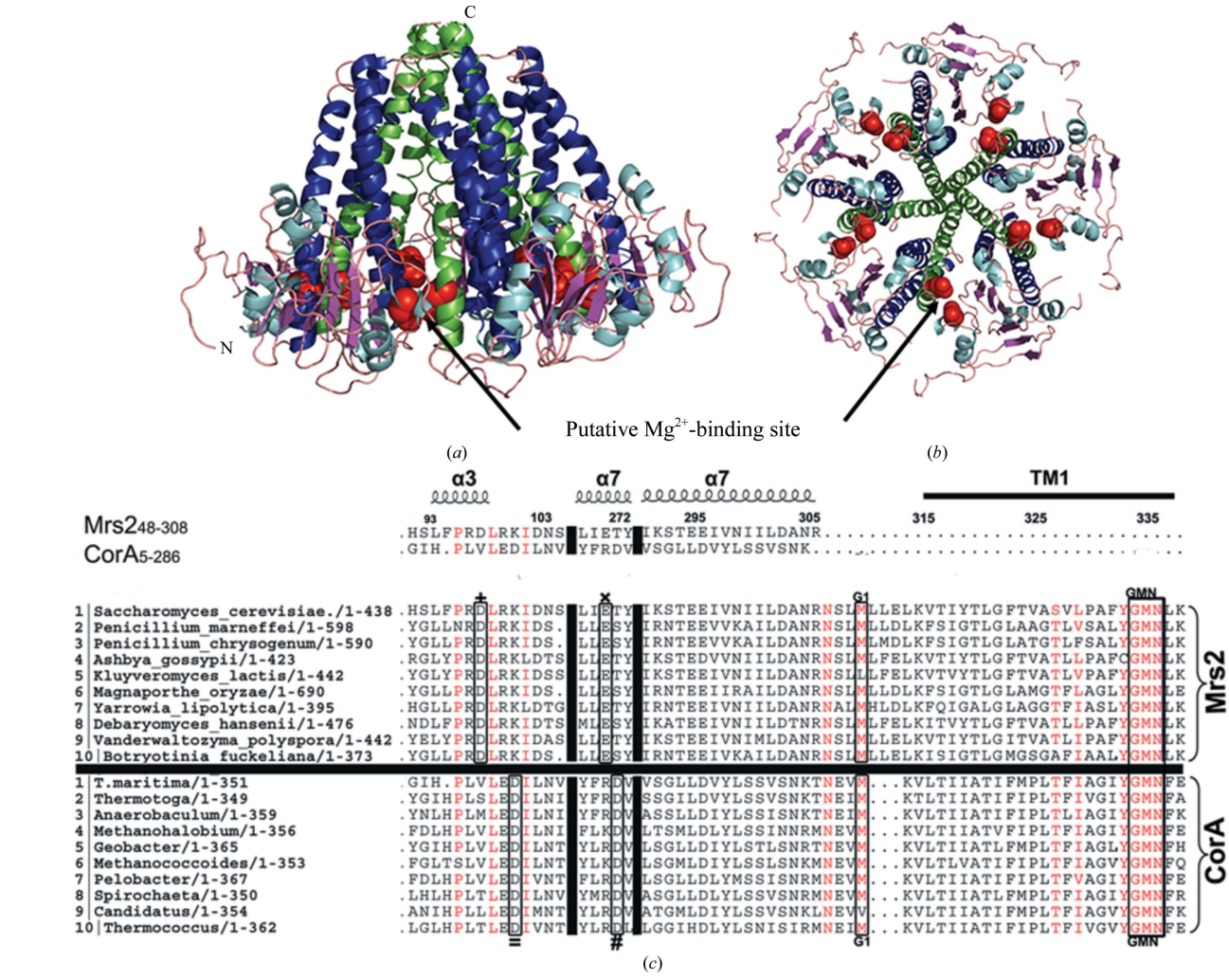

Figure 2
Models of the Mrs2 funnel and pentamer. (*a*) Side view of the pentameric funnel model of $Mrs2_{48–308}$ using Tm-CorA as template. The putative Mg^{2+}-binding site is mapped in red. (*b*) Bottom view of the pentameric funnel model with the putative Mg^{2+}-binding site mapped in red. (*c*) Structure-based sequence alignment of $Mrs2_{48–308}$ and Tm-CorA (PDB entry 2iub). The first two sequences belonging to the structures of $Mrs2_{48–308}$ and Tm-CorA are followed by ten sequences of eukaryotic Mrs2 and ten sequences of prokaryotic CorA channels from different species. Identical residues between Mrs2 and Tm-CorA channels are shown in red. The gaps owing to residues that were omitted from the sequence alignment are represented by two vertical solid black lines corresponding to residues 105–267 and 273–289, respectively, in Mrs2. In the case of Tm-CorA these represent residues 94–249 and 255–272, respectively. The sequences of the two phyla are separated by a horizontal black solid line. The average sequence identity between the prokaryotic species used in the alignment is about 53%, while that between eukaryotic species is about 52%. The conserved signature sequence GMN is boxed. Residues of the putative Mg^{2+}-binding site in eukaryotes, *i.e.* Asp97 and Glu270, are boxed and are denoted by + and × symbols. The prokaryotic Mg^{2+}-binding site formed by Asp89 and Asp253 is boxed and is denoted by = and # symbols in the sequence alignment. The residues involved in formation of the hydrophobic gate, *i.e.* Met309 in the case of the Mrs2 channel and Met291 in the case of the Tm-CorA channel, are boxed and are denoted by G1 in the sequence alignment. The secondary structure derived from $Mrs2_{48–308}$ is shown above the sequences. The residues embedded in the first transmembrane helix (TM1) are represented by a black solid line. (*d*) Side view of the pentameric Mrs2 model. The C-terminal triple coiled coil is coloured magenta, the N-terminal $\alpha/\beta/\alpha$ domain green and transmembrane helices TM1 and TM2 grey.

residues in the tip region (Lunin *et al.*, 2006). For $Mrs2_{48–308}$, $\alpha5$ and $\alpha6$, corresponding to the willow helices of Tm-CorA, contain three acidic residues compared with ten in Tm-CorA. In Tm-CorA there is also an extended loop between C2 and C3 that protrudes like the willow helices towards the membrane surface. The tip of this loop in Tm-CorA has a very high density of aspartic and glutamic acid residues (Maguire, 2006). In contrast, the C2 and C3 strands of $Mrs2_{48–308}$ are shorter and the loop that intercalates between them does not protrude towards the willow helices nor does it harbour any acidic residues (Figs. 1*c* and 1*e*).

To determine the structural neighbours of $Mrs2_{48–308}$, we used the web-based *DALI* server (Holm & Sander, 1996), which identified the following structures with *Z*-scores greater than 9: (i) *T. maritima* divalent metal-ion channel Tm-CorA (PDB entry 2iub; Eshaghi *et al.*, 2006), (ii) *V. parahaemolyticus* RIMD cytoplasmic domain of zinc channel Vp-ZntB (PDB entry 3ck6; Tan *et al.*, 2009), (iii) *S. enterica* serovar Typhimurium zinc channel (StZntB; PDB entry 3nwi; Q. Wan, B. Gorzelle, J. Fairman, M. Fuente, F. Homammed, C. Dealwis & M. Maguire, unpublished work), (iv) *Dictyostelium discoideum* STAT protein (PDB entry 1uus; Soler-Lopez *et al.*, 2004) and (v) *E. coli* pore-forming toxins (PDB code 2wcd; Mueller *et al.*, 2009). The molecular functions of the latter two hits are clearly different from Mrs2 and its prokaryotic counterparts and were discarded from further analyses. All of the above structures have low sequence similarity to *S. cerevisiae* Mrs2, and only Tm-CorA was identified in a *BLAST* (Altschul *et al.*, 1990) search against the Mrs2 sequence.

A detailed structural comparison (Supplementary Fig. S3) clearly shows that the prokaryotic proteins Tm-CorA and Vp-ZntB are structurally more similar to each other than to the eukaryotic protein $Mrs2_{48–308}$. Vp-ZntB also contains a mixed seven-stranded β-sheet that is clearly similar to that of Tm-CorA but differs from the six-stranded sheet of $Mrs2_{48–308}$.

3.4. Model of the Mrs2 pentamer

While the N-terminal domain $Mrs2_{48–308}$ is clearly different from the intracellular domain of Tm-CorA, both Mrs2 and CorA are pentameric. Under the assumption that the pentameric organization of Mrs2 and CorA is similar, we generated a model of the pentameric funnel from the structure of monomeric $Mrs2_{48–308}$ in order to find possible similarities and differences.

We first generated a model of the pentameric funnel from the structure of monomeric $Mrs2_{48–308}$ by superimposing $Mrs2_{48–308}$ onto the helical domains of Tm-CorA. Multiple sequence alignment based on the manually audited structure-based sequence alignment between $Mrs2_{48–308}$ and Tm-CorA (Fig. 2*c*) showed that eukaryotic Mg^{2+} channels consistently display a three-amino-acid insertion after the position corresponding to Met291 in prokaryotic channels, resulting in an extended $\alpha7$ helix. We generated the model of the Mrs2 pentamer, including the transmembrane helices, starting from the funnel model and extending the sequence (by homology modelling) to the C-terminal TM1 and TM2 α-helices (Fig. 2*d*). The three amino-acid residues of the Mrs2 insertion were modelled in a helical conformation as suggested by secondary-structure prediction analysis.

In a functional pentamer, each protomer makes contacts with two adjacent subunits. Our structural analysis of the $Mrs2_{48–308}$ funnel model based on the Tm-CorA structure shows five hydrogen-bonding interactions and one salt bridge. The residues involved in the formation of the salt bridge are Glu295 of one protomer and Lys291 of an adjacent protomer. The interacting residues belong to the $\alpha7$ stalk helix of one subunit, the $\alpha7$ stalk helix of the adjacent subunit and the tip of the $\alpha5$ and $\alpha6$ willow helices.

Conversely, there are 16 hydrogen bonds and 15 salt bridges in Tm-CorA (PDB entry 2bbj; Lunin *et al.*, 2006) and eight hydrogen bonds and eight salt bridges stabilizing the funnel of the Vp-ZntB channel (PDB entry 3ck6; Tan *et al.*, 2009). Although the stereochemistry of the interface of the $Mrs2_{48–308}$ funnel was not optimized, the presence of remarkably fewer hydrogen bonds and salt bridges compared with Tm-CorA and Vp-ZntB might explain the higher sensitivity of $Mrs2_{48–308}$ to elevated salt concentrations, where it is monomeric. A very similar sensibility of the pentameric oligomeric state to high ionic strength has also been observed for St-ZntB (Wan *et al.*, 2011).

Analysis of the electrostatic surface potential of the structure of $Mrs2_{48–308}$ showed that the $\alpha7$ helices forming the inner wall of the pentameric funnel are lined along their lengths with negatively charged or hydroxyl-bearing residues (Fig. 3). Such an arrangement exists in other monovalent cation (KcsA) and divalent cation (CorA and ZntB) channels and has been proposed to constitute an electrostatic sink that increases local ion concentrations (Roux & MacKinnon, 1999).

Inspection of structure-based multiple sequence alignment together with analysis of the Mrs2 pentamer model identified important residues involved in the formation of hydrophobic gates and in propagation of Mg^{2+} across the ion-conduction pathway in Mrs2-type channels, as described below.

3.5. Hydrophobic gates in Mrs2

The pentameric Mrs2 model shows a narrow constriction of the pore at residue Met309 (Fig. 4*a*), which is highly conserved amongst the members of the Mrs2 family (Fig. 2*c*). This amino acid corresponds to Met291 in Tm-CorA (Fig. 4*a*) which, together with Leu294, has been proposed to form a hydrophobic gate by creating a strong energetic barrier to ion permeation (Svidova *et al.*, 2010; Lunin *et al.*, 2006; Chakrabarti *et al.*, 2010). This gate is at the membrane–cytoplasmic interface, with Met291 being cytoplasmic and Leu294 being membrane-embedded (Lunin *et al.*, 2006). In the structure of Mj-CorA a 'hydrophobic lock' formed by two lysines and one methionine was observed, which in the closed state impedes even the movement of water molecules (Guskov *et al.*, 2012). From *TMpred* analysis (*Prediction of Transmembrane Regions and Orientation*; http://www.ch.embnet.org/software/TMPRED_form.html) of the primary sequence of *S. cerevisiae* Mrs2, the first transmembrane helix comprises residues

Val315–Leu336, while Met309 is predicted to be located in the matrix like Met291 in Tm-CorA.

The first residue of Mrs2 predicted to be in TM1 is Val315, which is six positions or a 1.5 α-helix turn downstream of the main gate residue Met309, and in the alignment corresponds to the second gating residue Leu294 in Tm-CorA (Fig. 2*c*). Supposing the α-helical conformation of the three-residue insertion in the stalk helix in Mrs2, the Val315 side chain does not face the pore but rather the neighbouring TM1 α-helix (Fig. 4*a*). The pentameric Mrs2 model and the sequence alignment suggest that the highly conserved Leu313 could be the candidate for a second gating position in Mrs2 (Fig. 4*b*), corresponding to Leu294 in Tm-CorA. This residue is highly conserved in eukaryotic Mg^{2+} channels (Fig. 2*c*), implying its functional importance. Furthermore, the sequence separation between residues Met291 and Leu294 in Tm-CorA is slightly different from the separation between Met309 and Leu313 in Mrs2.

Several gating mechanisms, which require complex structural rearrangements and are not limited to a few gating residues, have been proposed for CorA. Guskov and coworkers proposed that the passage of a partially hydrated ionic Mg^{2+} could be regulated by the degree of polarity of the pore, which might be adjusted by rotations of TM1 around its axis (Guskov *et al.*, 2012). Alternatively, Chakrabarti and coworkers hypothesized an iris-like mechanism according to which the membrane-pore bottleneck would be shortened and widened by a decrease in the intercellular concentration of Mg^{2+} (Chakrabarti *et al.*, 2010). It would be too daring to conclude that these gating mechanisms are compatible with our pentameric model of Mrs2 and further studies are necessary to obtain a deeper understanding of the chemical mechanisms that allow the pore to open/close.

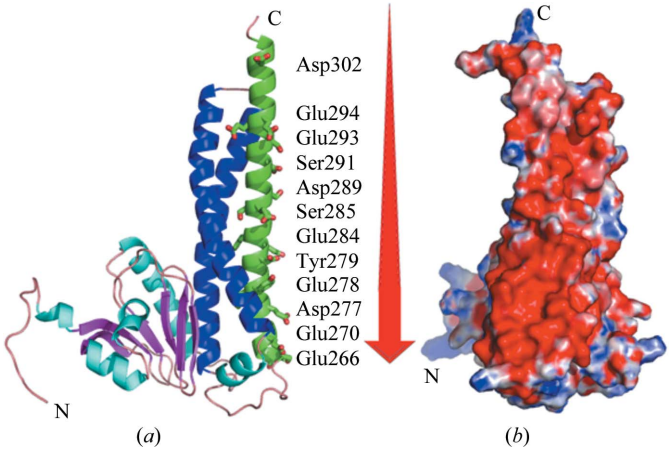

Figure 3
The inner wall of the Mrs2 funnel is negatively charged. (*a*) $Mrs2_{48–308}$ is represented as ribbons and the side chains of the negatively charged or hydroxyl-bearing residues of helix α7 that make up the inner side of the pore are represented as sticks. (*b*) Electrostatic surface-potential analysis of $Mrs2_{48–308}$ generated by *APBS*. Views are from the helix forming the inner wall of the funnel (red, negatively charged; blue, positively charged; white, uncharged). The red arrow shows the gradual increase in negative charge from top to bottom. All structural figures were created with *PyMOL* (http://www.pymol.org/).

By limiting our attention to Met309, which is most likely to sterically hinder the route of Mg^{2+} along the pore, we engineered several mutations and analyzed their physiological effects. Met309 was mutated to three amino acids with disparate properties with regard to size and charge: the small glycine, the negatively charged glutamic acid and the bulky phenylalanine. The effects of these mutations were monitored by growth-complementation assays and by using mag-fura-2 measurements of the Mg^{2+} influx into mitochondria.

In growth tests, all three mutations at Met309 location impaired growth on nonfermentable carbon sources, indicating that they had a considerable effect on Mg^{2+} homeostasis in mitochondria. The Met309Gly mutant had the most dramatic effect (Figs. 5*a* and 5*b*).

The greatest decrease in ionic Mg^{2+} uptake was observed in the Met309Phe variant (Fig. 5*b*), which is attributed to its bulky side chain narrowing the pore at this position. The Met309Gly mutant exerted the highest degree of deregulation with regard to the gating of the channel. Exchange of Met309 for Gly resulted in a considerably stronger influx compared with the wild-type protein and significantly elevated the final steady-state Mg^{2+} concentration (Fig. 5*b*). Particularly strong uptake was observed after the initial addition of ionic

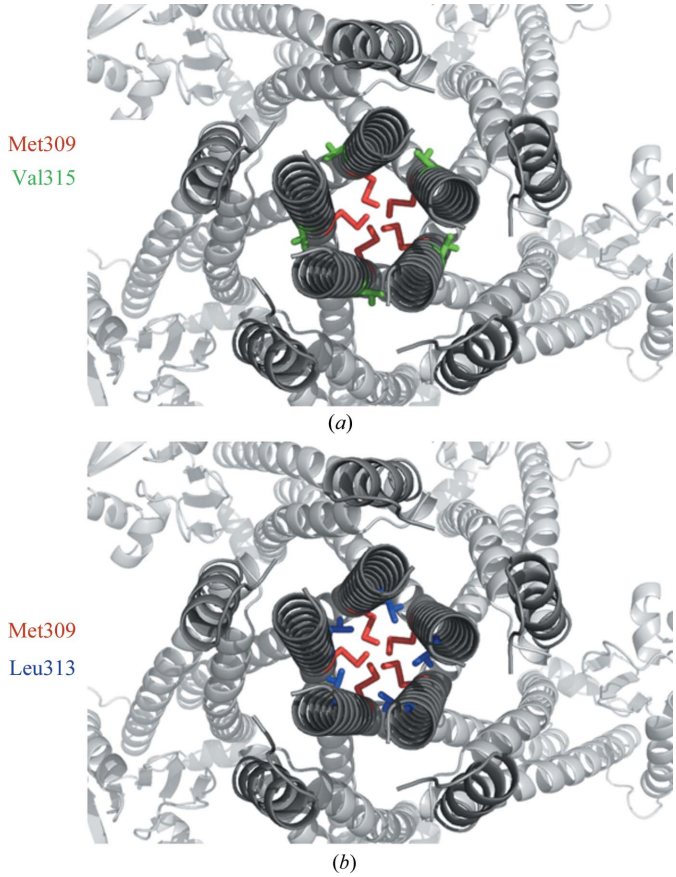

Figure 4
Putative hydrophobic gates in Mrs2. (*a*) Top view of the model of the Mrs2 channel showing the putative first hydrophobic gate residue Met309 (red) and Val315 pointing towards the neighbouring TM1 helix (green). (*b*) Top view of the model of the Mrs2 channel showing the putative first hydrophobic gate residue Met309 (red) and the second Leu313 (blue).

Mg^{2+}, and plateau levels were less pronounced compared with the wild-type control (Fig. 5*b*). The channel was able to close the ion-conduction pathway to a limited extent (Fig. 5*b*), suggesting that in the Met309Gly mutant the pore is wide and cannot close properly owing to the absence of the glycine side chain. An effect similar to that of the Met309Gly mutant was observed for Met309Glu, which displayed higher final steady-state Mg^{2+} levels compared with the wild type (Fig. 5*b*). This effect might be caused by the formation of a negatively charged ring in the pentamer, eliciting more robust transport owing to increased electrostatic attraction of the Mg^{2+} ion.

In contrast, mutations of Val315, a residue that in our pentamer model does not point into the pore but towards a neighbouring TM1 helix (Fig. 4*a*), to Glu and Phe had no significant effect on growth on nonfermentable carbon sources (Fig. 5*c*). Mg^{2+} uptake by the Glu mutant was comparable to that of wild-type Mrs2, a fact that can be rationalized by assuming that Glu side chains might be (partially) protonated in a hydrophobic environment. The bulky Phe residue was well tolerated and did not impair ion conduction to such an extent as to lead to a substantial reduction in ionic Mg^{2+} uptake (Fig. 5*d*). This is not surprising as this residue is also found at position 315 in some naturally occurring sequences, suggesting that a bulkier residue can be accommodated at this location (Fig. 2*c*).

A third type of mutation, Val315Gly, slightly reduced the growth but did not cause a significant change in Mg^{2+} uptake as assessed by mag-fura-2 measurements (Fig. 5*d*). Taken

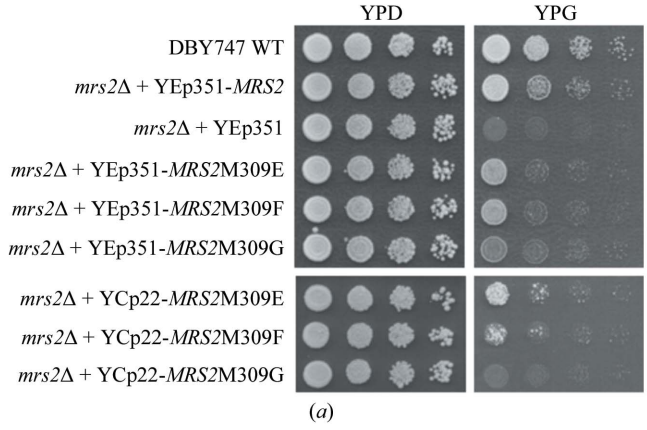

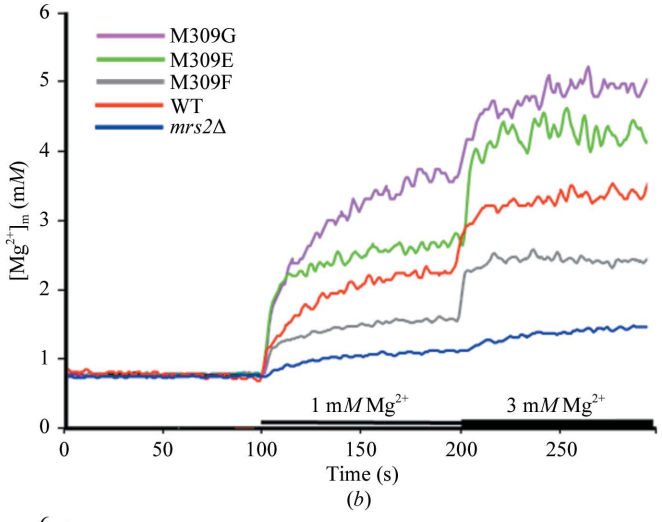

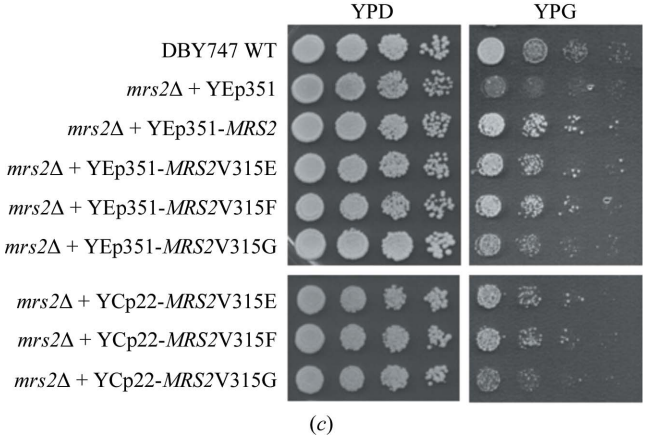

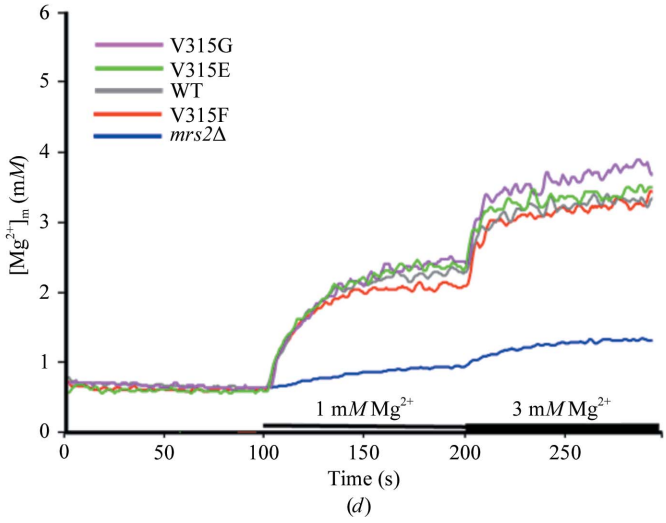

Figure 5
Mutations of the hydrophobic gate (Met309) of Mrs2 impair growth on nonfermentable carbon sources and alter the transport activity of the channel, while mutations of Val315 do not alter the channel activity. (*a*) Growth phenotypes of *S. cerevisiae* strain DBY747 *mrs2*Δ expressing wild-type *MRS2* and the corresponding *MRS2* mutant variants from the high-copy-number vector YEp351 or the low-copy-number vector YCp22. Serial dilutions of the different strains were spotted on fermentable (YPD) and nonfermentable (YPG) substrates and grown for 3 or 6 d, respectively. (*b*) $[Mg^{2+}]_e$-dependent changes in $[Mg^{2+}]_m$ in mitochondria of *mrs2*Δ cells and cells expressing WT *MRS2* or the mutant variants. Isolated mitochondria were loaded with the Mg^{2+}-sensitive dye mag-fura-2 and changes in the intra-mitochondrial free Mg^{2+} concentration upon addition of Mg^{2+} to the nominally Mg^{2+}-free buffer, as indicated in the figure, were determined. Representative recordings of four individual measurements are shown. (*c*) Serial dilutions of DBY747 WT and DBY747 *mrs2*Δ cells transformed with the vectors Yep351 and YCp22 expressing *MRS2* or different mutant variants of Val315 were spotted on fermentable (YPD) or nonfermentable (YPG) plates and incubated at 301 K for 3 or 6 d, respectively. (*d*) $[Mg^{2+}]_e$-dependent changes in $[Mg^{2+}]_m$ in mitochondria of DBY 747 *mrs2*Δ cells expressing WT *MRS2* or mutant variants of Val315. Representative curve traces of three individual measurements are shown. The curves were smoothened using the Golay–Savitzky algorithm (with a series of 100 data points; Savitzky & Golay, 1964).

together, the above observations confirm residue Met309 as the possible gating residue in Mrs2, probably equivalent to Met291 in Tm-CorA, and suggest that Val315 does not face the pore.

3.6. Putative Mg^{2+}-sensing sites in Mrs2

It has been proposed that Mg^{2+} influx is regulated by the intracellular ionic Mg^{2+} concentration in CorA. Mg^{2+} cations can bridge pairs of adjacent N-terminal globular domains and a decrease in the cytosolic Mg^{2+} concentration would relax the reciprocal orientation of the five N-terminal globular domains, with a consequent opening of the channel. Although the detailed mechanism of the relationship between the dynamics of the movements of the N-terminal domains and the pore gating is still under discussion (Chakrabarti *et al.*, 2010; Guskov *et al.*, 2012; Palombo *et al.*, 2012; Pfoh *et al.*, 2012), there is some agreement about the fact that Mg^{2+} cations may interact, perhaps not directly but *via* water molecules, with two adjacent N-terminal domains of CorA. The Mg^{2+}-binding sites are generally termed 'divalent cation sensor' (DCS) sites and although several low-affinity Mg^{2+}-binding sites have been observed in molecular-dynamics simulations (Chakrabarti *et al.*, 2010), a single binding site has been observed crystallographically *in vitro* (Eshaghi *et al.*, 2006; Payandeh & Pai, 2006; Lunin *et al.*, 2006; Payandeh *et al.*, 2008; Pfoh *et al.*, 2012; Guskov *et al.*, 2012). It involves two aspartates, Asp89 and Asp253, one from one domain and the other from an adjacent domain.

Based on structural comparison between Tm-CorA and our model of the Mrs2 funnel, we identified candidate amino-acid residues that could form a DCS site in Mrs2: Asp97 from one subunit and Glu270 from an adjacent subunit (Figs. 6*a* and 6*b*). By sequence alignment of eukaryotic Mrs2 homologues, Asp97 and Glu270 are highly conserved throughout the entire family and equivalent residues exist in the prokaryotic CorA family (Fig. 2*c*). In Mrs2, Asp97 is located in the α3 helix, corresponding to Asp89 of Tm-CorA (Fig. 6*c*), while Glu270 lies in the N-terminus of α7, corresponding to Asp253 in Tm-CorA (Fig. 6*d*). In this structural analysis, we could not confidently identify residues that might constitute additional DCS sites.

In the initial crystallization conditions of $Mrs2_{48–308}$ no Mg^{2+} was present, but we also obtained crystals with 1.5 m*M* magnesium chloride and 1.5 m*M* cobalt chloride. The structures of Mg^{2+}-soaked and Co^{2+}-soaked $Mrs2_{48–308}$ crystals and of Mg^{2+} and Co^{2+} cocrystals did not reveal bound metal ions and the structures were essentially identical to the native crystal structure. The absence of cations bound to the monomeric $Mrs2_{48–308}$ is in agreement with the notion that the DCS sites are composed of ligands from adjacent subunits in the pentamer, implying that a single subunit cannot bind divalent ions with high affinity.

Furthermore, the potential Mg^{2+} ligand Asp97 of Mrs2 was mutated to Ala, Phe and Trp. Deletion of *MRS2* causes a growth defect on nonfermentable carbon sources and abolishes Mg^{2+} influx into mitochondria (Kolisek *et al.*, 2003; Wiesenberger *et al.*, 1992). Strain DBY747 *mrs2*Δ was transformed with the high-copy-number vector YEp351 or with the centromeric plasmid YCp22 harbouring the mutated *MRS2* variants and, as controls, wild-type *MRS2* and the empty vector (Supplementary Fig. S4). The cells expressing the mutant variants did not exhibit notable growth defects (Fig. 7*a*). Accordingly, no significant differences in Mg^{2+} uptake between wild-type Mrs2 and the mutant proteins in isolated mitochondria were observed (Fig. 7*b*).

Based on the high conservation of Asp97 throughout the Mrs2 subfamily, the lack of an effect is noteworthy. It might imply that the mechanism of cytosolic Mg^{2+} sensing of Mrs2 is different from that of CorA. Alternatively, one may also speculate that the mutation of a single residue is insufficient to prevent the reversible Mg^{2+} binding by Mrs2. On the basis of a molecular-dynamics simulation that showed several low-affinity Mg^{2+}-binding sites in Tm-CorA (Chakrabarti *et al.*, 2010), it is also possible to argue that several Mg^{2+}-binding sites can also exist in Mrs2. Similarly, the DCS sites of Mj-CorA are not well defined and were proposed to consist of several negatively charged amino-acid side chains and main-chain carbonyl groups forming Mg^{2+}-binding grooves

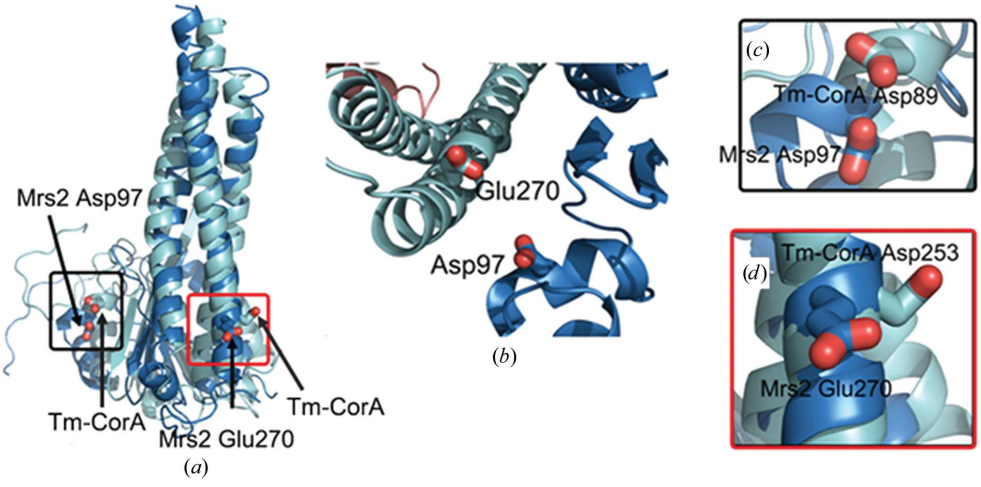

Figure 6
The putative Mg^{2+}-binding site in Mrs2. (*a*) Superposition of $Mrs2_{48–308}$(blue) and Tm-CorA (cyan) soluble domains showing the Mg^{2+}-binding site of Tm-CorA and the putative Mg^{2+}-binding site of $Mrs2_{48–308}$. The coloured boxes (*c*, *d*) show the residues involved in Mg^{2+} sensing. (*b*) The putative Mg^{2+}-binding pocket featuring Asp97 from one monomer (blue) and Glu270 from an adjacent subunit (cyan) in a proposed pentameric model. (*c*) The Mg^{2+}-binding residue Asp89 of Tm-CorA and the corresponding putative Mg^{2+}-binding residue Asp97 of $Mrs2_{48–308}$. (*d*) The Mg^{2+}-binding residue Asp253 of Tm-CorA and the corresponding putative Mg^{2+}-binding residue Glu270 of $Mrs2_{48–308}$.

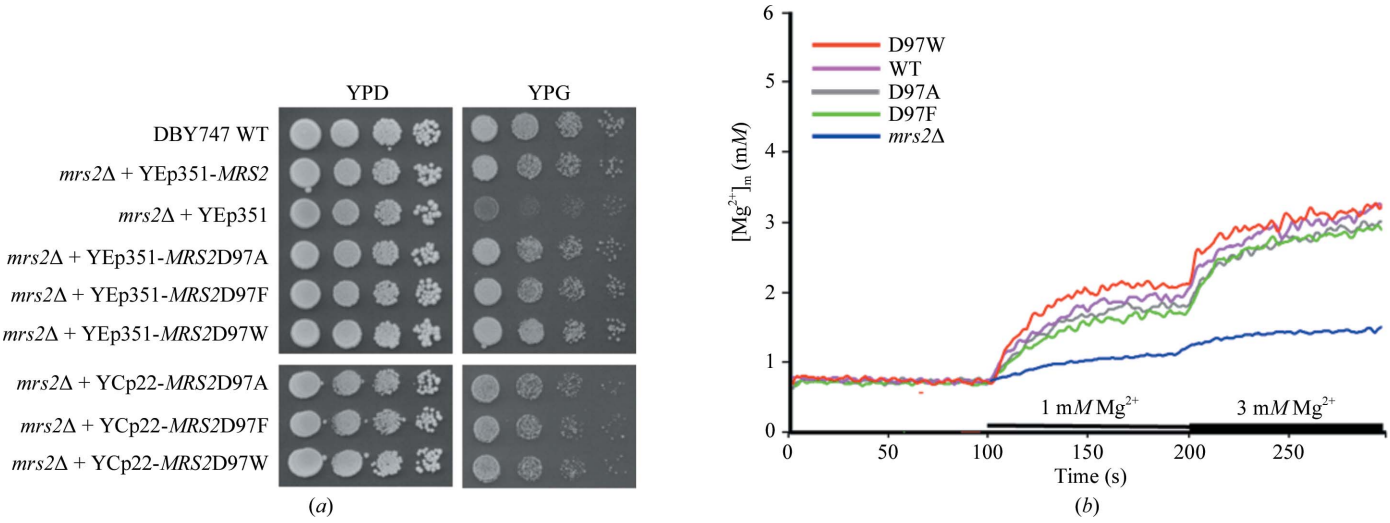

Figure 7
Mutation of Asp97 of a putative Mg^{2+}-binding site in Mrs2 does not influence the regulation of the channel. (*a*) Growth phenotypes of *S. cerevisiae* strain DBY747 *mrs2*Δ expressing *MRS2* variants harbouring mutations in the Asp97 site from the high-copy-number vector YEp351 or the low-copy-number vector YCp22. Deletion of *MRS2* leads to a growth defect on nonfermentable carbon sources. In order to assess mitochondrial function in cells expressing the different Mrs2 mutant variants, growth tests were performed on fermentable (glucose as carbon source; YPD) and nonfermentable (YPG) plates containing nonfermentable glycerol as the sole carbon source. Serial dilutions of yeast cultures were spotted on YPD or YPG plates and incubated at 291 K for 3 or 6 d, respectively. (*b*) $[Mg^{2+}]_e$-dependent changes in $[Mg^{2+}]_m$ in DBY 747 *mrs2*Δ mitochondria expressing *MRS2* or the mutant variants were determined. Representative curve traces of four individual measurements are shown. The curves were smoothened using the Golay–Savitzky algorithm (with a series of 100 data points; Savitzky & Golay, 1964).

(Guskov *et al.*, 2012). Further studies are necessary to understand Mg^{2+} sensing by Mrs2 and its effects on mitochondrial physiology.

3.7. Effect of metal ions on the protease susceptibility of pentameric $Mrs2_{48–308}$

Payandeh and Pai showed that cations in the protomer interface stabilize Tm-CorA but are not required to maintain its pentameric state (Payandeh & Pai, 2006). Furthermore, they demonstrated that Tm-CorA becomes resistant to trypsin in a divalent cation-dependent manner, in which the presence of ions renders the conformation trypsin-resistant, presumably reflecting the closed state of the channel. To determine whether $Mrs2_{48–308}$ undergoes conformational changes in the presence of divalent cations, we performed a protease-susceptibility assay in the presence and absence of Mg^{2+} and Co^{2+} ions.

Prior to this experiment, $Mrs2_{48–308}$ was dialyzed against a low ionic strength buffer to induce the formation of pentamers and was subsequently incubated with various concentrations of Mg^{2+}, Co^{2+}, EDTA and trypsin (Fig. 8). In the presence of EDTA the protein was protected from protease digestion. Conversely, only high concentrations of Co^{2+} rendered $Mrs2_{48–308}$ less susceptible to trypsin cleavage, whereas the presence of Mg^{2+} did not, irrespective of the incubation time (Fig. 8). The reactions were performed at 277 and 310 K for 4 and 15 h.

These results suggest that Mrs2 might adopt two distinct conformations in an Mg^{2+}-dependent manner, in which the closed conformation (in the presence of Mg^{2+}) appears to be more susceptible to protease cleavage compared with the open conformation (in the presence of EDTA). This differential susceptibility compared with Tm-CorA implicates distinct local conformations and distinct conformational changes in the N-terminal domains of the two types of channels. Differences between the folds of the two domains might

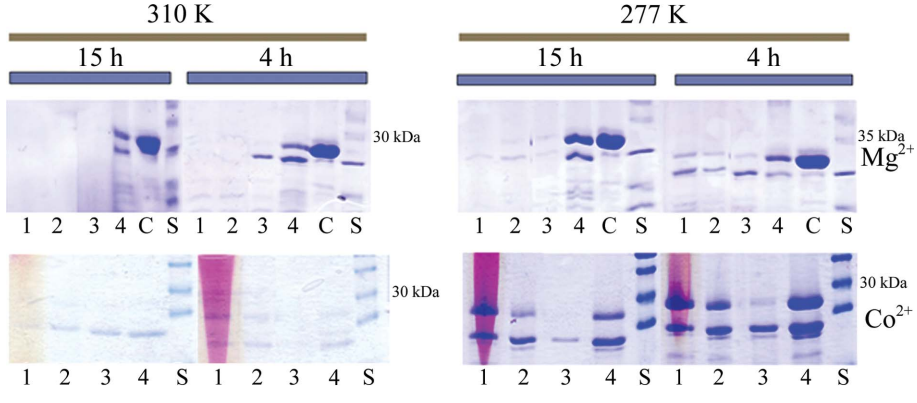

Figure 8
Protease-susceptibility assay. Trypsin susceptibility of $Mrs2_{48–308}$ after 4 h (right) and 15 h (left). Reactions were performed as described in §2. Control samples (C) for the different experimental conditions and the molecular-weight ladder (S) are shown. The different tested conditions in the protease-susceptibility assay are (1) 20 m*M* Mg^{2+} (or 20 m*M* Co^{2+}), (2) 5 m*M* Mg^{2+} (or 5 m*M* Co^{2+}), (3) 5 m*M* EDTA, (4) 20 m*M* EDTA. The temperature is shown above the golden bar, *i.e.* 277 K (right) and 310 K (left).

be related to the varying responses and patterns with regard to protease susceptibility.

4. Conclusions

In summary, this study provides the first molecular view of the regulatory N-terminal moiety of the eukaryotic Mg^{2+} channel Mrs2 from *S. cerevisiae*. Together with structure-based mutagenesis and functional analysis *in vivo*, the study provides insights into the gating and regulation of Mrs2. The study identified candidate residues implicated in divalent cation binding and residues involved in formation of the hydrophobic gate. Our observations suggest a high degree of regulation of the Mrs2 channel similar to Tm-CorA, which interestingly has recently been reported to preferentially transport Co^{2+} and not Mg^{2+} (Xia *et al.*, 2011). The high inside negative membrane potential of mitochondria attracting the positively charged Mg^{2+} ion requires fine monitoring of the intramitochondrial ion concentration at more than one site and stringent control of ion permeation to ensure normal mitochondrial function.

We acknowledge the ESRF, Grenoble for the provision of synchrotron radiation. MBK, GS and SS were recipients of a PhD fellowship from Austrian Science Fund FWF (P20141) and from Vienna Science and Technology Fund WWTF (LS05021). MBK was partially supported by University of Vienna funds. We also acknowledge the BIN-III initiative of the Austrian GEN-AU for financial support.

References

Altschul, S. F., Gish, W., Miller, W., Myers, E. W. & Lipman, D. J. (1990). *J. Mol. Biol.* **215**, 403–410.
Bui, D. M., Gregan, J., Jarosch, E., Ragnini, A. & Schweyen, R. J. (1999). *J. Biol. Chem.* **274**, 20438–20443.
Chakrabarti, N., Neale, C., Payandeh, J., Pai, E. F. & Pomès, R. (2010). *Biophys. J.* **98**, 784–792.
Cowan, J. A. (1991). *Inorg. Chem.* **30**, 2740–2747.
Cowan, J. A. (1998). *Chem. Rev.* **98**, 1067–1088.
Cowan, J. A., Ohyama, T., Howard, K., Rausch, J. W., Cowan, S. M. & Le Grice, S. F. (2000). *J. Biol. Inorg. Chem.* **5**, 67–74.
Dann, C. E. III, Wakeman, C. A., Sieling, C. L., Baker, S. C., Irnov, I. & Winkler, W. C. (2007). *Cell*, **130**, 878–892.
Eshaghi, S., Niegowski, D., Kohl, A., Martinez Molina, D., Lesley, S. A. & Nordlund, P. (2006). *Science*, **313**, 354–357.
Froschauer, E. M., Kolisek, M., Dieterich, F., Schweigel, M. & Schweyen, R. J. (2004). *FEMS Microbiol. Lett.* **237**, 49–55.
Gouet, P., Robert, X. & Courcelle, E. (2003). *Nucleic Acids Res.* **31**, 3320–3323.
Guex, N. & Peitsch, M. C. (1997). *Electrophoresis*, **18**, 2714–2723.
Guskov, A., Nordin, N., Reynaud, A., Engman, H., Lundbäck, A.-K., Jong, A. J. O., Cornvik, T., Phua, T. & Eshaghi, S. (2012). *Proc. Natl Acad. Sci. USA*, **109**, 18459–18464.
Holm, L. & Sander, C. (1996). *Science*, **273**, 595–603.
Joosten, K., Cohen, S. X., Emsley, P., Mooij, W., Lamzin, V. S. & Perrakis, A. (2008). *Acta Cryst.* D**64**, 416–424.
Jung, J. & Lee, B. (2000). *Protein Eng.* **13**, 535–543.
Kabsch, W. (2010). *Acta Cryst.* D**66**, 125–132.
Kehres, D. G., Lawyer, C. H. & Maguire, M. E. (1998). *Microb. Comput. Genomics*, **3**, 151–169.
Kehres, D. G. & Maguire, M. E. (2002). *Biometals*, **15**, 261–270.
Khan, M. B., Sjöblom, B., Schweyen, R. J. & Djinović-Carugo, K. (2010). *Acta Cryst.* F**66**, 658–661.
Kolisek, M., Zsurka, G., Samaj, J., Weghuber, J., Schweyen, R. J. & Schweigel, M. (2003). *EMBO J.* **22**, 1235–1244.
Larkin, M. A., Blackshields, G., Brown, N. P., Chenna, R., McGettigan, P. A., McWilliam, H., Valentin, F., Wallace, I. M., Wilm, A., Lopez, R., Thompson, J. D., Gibson, T. J. & Higgins, D. G. (2007). *Bioinformatics*, **23**, 2947–2948.
Li, L., Tutone, A. F., Drummond, R. S., Gardner, R. C. & Luan, S. (2001). *Plant Cell*, **13**, 2761–2775.
Lunin, V. V., Dobrovetsky, E., Khutoreskaya, G., Zhang, R., Joachimiak, A., Doyle, D. A., Bochkarev, A., Maguire, M. E., Edwards, A. M. & Koth, C. M. (2006). *Nature (London)*, **440**, 833–837.
Maguire, M. E. (2006). *Curr. Opin. Struct. Biol.* **16**, 432–438.
Morris, R. J., Perrakis, A. & Lamzin, V. S. (2003). *Methods Enzymol.* **374**, 229–244.
Mueller, M., Grauschopf, U., Maier, T., Glockshuber, R. & Ban, N. (2009). *Nature (London)*, **459**, 726–730.
Palombo, I., Daley, D. O. & Rapp, M. (2012). *J. Biol. Chem.* **287**, 27547–27555.
Payandeh, J., Li, C., Ramjeesingh, M., Poduch, E., Bear, C. E. & Pai, E. F. (2008). *J. Biol. Chem.* **283**, 11721–11733.
Payandeh, J. & Pai, E. F. (2006). *EMBO J.* **25**, 3762–3773.
Pearson, W. R. (1991). *Genomics*, **11**, 635–650.
Pfoh, R., Li, A., Chakrabarti, N., Payandeh, J., Pomès, R. & Pai, E. F. (2012). *Proc. Natl Acad. Sci. USA*, **109**, 18809–18814.
Quigley, G. J., Teeter, M. M. & Rich, A. (1978). *Proc. Natl Acad. Sci. USA*, **75**, 64–68.
Roux, B. & MacKinnon, R. (1999). *Science*, **285**, 100–102.
Savitzky, A. & Golay, M. J. E. (1964). *Anal. Chem.* **36**, 1627–1639.
Schock, I., Gregan, J., Steinhauser, S., Schweyen, R., Brennicke, A. & Knoop, V. (2000). *Plant J.* **24**, 489–501.
Soler-Lopez, M., Petosa, C., Fukuzawa, M., Ravelli, R., Williams, J. G. & Müller, C. W. (2004). *Mol. Cell*, **13**, 791–804.
Svidova, S., Sponder, G., Schweyen, R. J. & Djinović-Carugo, K. (2010). *Biochim. Biophys. Acta*, **1808**, 1587–1591.
Tan, K., Sather, A., Robertson, J. L., Moy, S., Roux, B. & Joachimiak, A. (2009). *Protein Sci.* **18**, 2043–2052.
Usón, I. & Sheldrick, G. M. (1999). *Curr. Opin. Struct. Biol.* **9**, 643–648.
Vonrhein, C., Blanc, E., Roversi, P. & Bricogne, G. (2007). *Methods Mol. Biol.* **364**, 215–230.
Walker, G. M., Birch-Andersen, A., Hamburger, K. & Kramhøft, B. (1982). *Carlsberg Res. Commun.* **47**, 205–214.
Wan, Q., Ahmad, M. F., Fairman, J., Gorzelle, B., de la Fuente, M., Dealwis, C. & Maguire, M. E. (2011). *Structure*, **19**, 700–710.
Wiesenberger, G., Waldherr, M. & Schweyen, R. J. (1992). *J. Biol. Chem.* **267**, 6963–6969.
Worlock, A. J. & Smith, R. L. (2002). *J. Bacteriol.* **184**, 4369–4373.
Xia, Y., Lundbäck, A.-K., Sahaf, N., Nordlund, G., Brzezinski, P. & Eshaghi, S. (2011). *J. Biol. Chem.* **286**, 16525–16532.
Zhang, T. & Mu, Y. (2012). *PLoS One*, **7**, e43872.
Zsurka, G., Gregán, J. & Schweyen, R. J. (2001). *Genomics*, **72**, 158–168.